EEET ECOLOGICAL ENGINEERING & ENVIRONMENTAL TECHNOLOGY

*Ecological Engineering & Environmental Technology*, 2026, 27(8), 512–531
https://doi.org/10.12912/27197050/225666
ISSN 2719–7050, License CC-BY 4.0

Received: 2026.06.30
Accepted: 2026.10.07
Published: 2026.08.01

# Integrating land cover dynamics and projections to assess surface drought susceptibility using frequency ratio and cellular automata in the Takkalasi Watershed

Nur Dwiyanti Utari[1], Andang Suryana Soma[2*], Ahmad Munir[3], Rahmat Syaeful[4]

[1] Regional Planning and Development Study Program, Graduate School, Hasanuddin University, Makassar, Indonesia
[2] Department of Forestry, Faculty of Forestry, Hasanuddin University, Makassar, Indonesia
[3] Department of Agricultural Technology, Faculty of Agricultural Technology, Hasanuddin University, Makassar, Indonesia
[4] Remote Sensing and Geographic Information System Study Program, Faculty of Vocational Studies, Hasanuddin University, Makassar, Indonesia
* Corresponding author's e-mail: s_andangs@unhas.ac.id

## ABSTRACT

Land cover degradation from increasing anthropogenic pressure is a key driver of rising surface drought susceptibility in watersheds, yet the spatial relationship between land cover dynamics and drought susceptibility distribution remains understudied in an integrated framework. This study examines historical land cover change in the Takkalasi Watershed, Barru Regency, South Sulawesi, from 2016 to 2025; projects land cover patterns through 2045; and maps surface drought susceptibility using an integrated approach. Land cover change was analyzed through supervised classification of Landsat 8 imagery, while the 2045 projection was generated using a Cellular Automata model in LanduseSim. Surface drought susceptibility was modeled using the frequency ratio (FR) method based on the drought susceptibility index (DSI), incorporating LST, NDVI, NDBI, precipitation, slope, soil texture, distance to river, hotspots, and land cover. Model validation used a 70:30 data split, with AUC-ROC evaluation conducted in SPSS. Results show that rice paddy and settlement classes experienced the greatest historical area increases, while dryland agriculture and shrubland declined most significantly. Projections for 2045 indicate a dramatic expansion of residential areas in the middle and lower watershed reaches. FR analysis identified building density, residential land cover, and rice paddies as the factors most strongly associated with elevated drought susceptibility. Approximately 28.63% of the watershed falls into the high-to-very-high susceptibility category, concentrated in the middle and lower reaches. The FR model demonstrated strong performance, with an AUC Success Rate of 0.807 and a Prediction Rate of 0.727. Rather than positioning FR-CA integration as a methodological innovation, this study frames its contribution as a reproducible, integrated assessment workflow linking historical land-cover dynamics, cellular automata-based projection, and drought susceptibility mapping for watershed-scale risk planning. The findings indicate that anthropogenic land-cover change is a key ecological pathway increasing surface drought susceptibility in the Takkalasi Watershed, providing a basis for ecological engineering interventions riparian and forest restoration, agroforestry, and infiltration enhancement and for local-level climate adaptation planning.

**Keywords:** land cover change, surface drought susceptibility, landscape transformation, frequency ratio, cellular automata, watershed management, Takkalasi Watershed.

## INTRODUCTION

Global land cover change has become one of the main drivers of ecosystem degradation and increased regional vulnerability to drought (Sterling et al., 2013). The conversion of forests and naturally vegetated lands into agricultural areas, settlements, and built-up areas significantly reduces the ecosystem's capacity to store water, increases surface runoff, and reduces infiltration into the soil (Yang et al., 2022). Uncontrolled land-cover changes, when combined with the intensifying pressures of climate change particularly in tropical regions and developing countries (Mahmood et al., 2014). These impacts not only threaten food security and water resources availability, but also disrupt the hydrological cycle and ecological functions (Akther et al., 2026).

In Indonesia, a tropical archipelago, land-cover change is accelerating alongside population growth, agricultural expansion, and massive infrastructure development (Banerjee, 2012). South Sulawesi Province is one of the regions that has experienced an increase in meteorological and hydrological droughts over the past decade, primarily driven by El Niño climate variability and the conversion of forests into agricultural land and built-up areas (Supari et al., 2016). These droughts have had widespread impacts on agricultural productivity, water supply, and the sustainability of river ecosystems in the region (Lu et al., 2019). Various studies in Sulawesi's river basins indicate that a decline in forest vegetation cover consistently increases the region's vulnerability to water deficits, particularly during increasingly prolonged dry seasons driven by climate anomalies (Hatta and Yuni, 2019)

This situation is particularly evident in the Takkalasi River Basin, Barru Regency, South Sulawesi. As one of the key river basins that plays a vital role in supporting agricultural activities and meeting the community's water needs, this region is experiencing intensive land-use changes due to anthropogenic activities, including the expansion of agricultural land and the growth of residential areas. These changes in land cover patterns can increase the risk of drought, particularly during the dry season, as reduced vegetation cover directly reduces water interception and retention capacity (Zhang et al., 2024). Nevertheless, a comprehensive understanding of historical trends in land-use change and future projections in the Takkalasi Watershed remains limited; therefore, a thorough spatiotemporal analysis is needed as the basis for adaptive watershed management planning.

The relationship between land cover change and drought vulnerability is complex and mutually reinforcing (Wilhite et al., 2014). A decline in vegetation cover reduces evapotranspiration and the soil's ability to retain water, thereby exacerbating water deficits during dry periods (Chen et al., 2020). Conversely, prolonged drought can accelerate land degradation and drive further changes in land cover, creating a negative feedback loop that worsens the watershed's the overall hydrological conditions. In this context, vulnerability to hydrometeorological disasters is not determined solely by climatic factors, but also by land-use dynamics and the adaptive capacity of ecosystems (Angeluccetti et al., 2014). Therefore, an integrated approach combining LULCC analysis and drought vulnerability modeling is crucial for predicting future impacts in tropical regions.

Various methods have been developed to analyze this issue spatially. The cellular automata (CA) model, implemented in the LanduseSim software, has proven effective at simulating the spatial dynamics of land cover change using transition rules and land-use change drivers, with a level of accuracy sufficient for long-term projections (Banerjee, 2012). Meanwhile, the frequency ratio (FR) method provides a simple yet accurate statistical approach to mapping drought vulnerability by linking historical drought events to relevant environmental factors (Li et al., 2017). These two approaches can complement each other within a spatio-temporal analysis framework for assessing drought vulnerability at the watershed scale.

Nevertheless, most research in Indonesia continues to treat land-use change analysis and drought modeling as separate lines of inquiry, rather than as components of an integrated hydro-ecological system. Studies that integrate long-term projections using cellular automata with Frequency Ratio-based susceptibility modeling statistically validated at the local watershed scale, particularly in South Sulawesi remain very limited (Triyatno et al., 2025). More specifically, few studies have linked historical land-cover trajectories with future drought-susceptibility patterns at the scale of individual tropical watersheds, leaving a scientific gap in spatially explicit, evidence-based guidance for adaptive watershed management (Hakiki et al., 2026).

Beyond the specific combination of methods, the scientific contribution of this study is positioned around an integrated hydro-ecological assessment framework that links historical land-cover dynamics, cellular automata-based future land-use projection, and frequency-ratio drought susceptibility mapping within a single, spatially explicit and reproducible workflow for a small, data-scarce tropical watershed. Rather than proposing a new statistical or simulation technique, the contribution of this study lies in demonstrating how this combined workflow generates spatially explicit, forward-looking evidence extending two decades beyond the observed record that is directly usable for watershed-scale risk-based planning, ecological engineering interventions such as riparian and forest-cover restoration prioritization, and local-level climate change adaptation strategies, consistent with recent calls for application-oriented, decision-relevant integration of land-use and hazard modelling in tropical river basins (Vahid and Aly, 2025; Triyatno et al., 2025).

This study aims to address this gap through three specific objectives: (1) to analyze historical land use/land cover (LULC) change in the Takkalasi watershed for the 2016–2025 period; (2) to project future LULC patterns through 2045 using a Cellular Automata model; and (3) to evaluate the influence of historical and projected landscape transformation on surface drought susceptibility, validated through receiver operating characteristic (ROC) analysis and the area under the curve (AUC) (Ghalehteimouri et al., 2022). This integrated approach is expected to provide a scientific basis for risk-based watershed management and the development of climate change adaptation strategies at the local level.

## MATERIALS AND METHODS

### Study area

The study area is located in the Takkalasi watershed, which administratively falls within Barru Regency, South Sulawesi Province, and encompasses two subdistricts: Balusu and Barru. The watershed covers of 9,317 ha, extending from the upstream region in the eastern mountains to its mouth at the Makassar Strait. Geographically, the study area is located at 4°18’6.55” – 4°25’21.67” S and 119°38’55.86” – 119°42’13.96” E. As shown in Figure 1, the study area map shows the location of the Takkalasi Watershed and its administrative boundaries.

### Historical land use/land cover analysis (2016–2025) and projection for 2045

Land cover data were generated via on-screen digitization of Landsat 8 imagery from 2016 and 2025, using a supervised classification approach. Scenes were selected from the dry-season period of each reference year to minimize cloud interference and shadow-related misclassification, and standard radiometric and atmospheric correction were applied prior to classification. [Author to confirm and insert here the exact acquisition dates, path/row identifiers, and cloud-cover percentage for the 2016 and 2025 Landsat 8 scenes used.] The band combination used was 6-5-4 (SWIR-NIR-RED) with a pixel resolution of 30 × 30 m, as shown in Figure 2. Resolution sharpening was performed through a pan-sharpening step using band 8 (panchromatic) to achieve a resolution of 15 × 15 m. The interpretation process accounted for nine elements of image interpretation: hue, size, shape, texture, pattern, elevation, shadow, location, and association. This approach was adopted to ensure accurate classification in land cover classes within the study area.

The accuracy of the interpretation results was assessed using a confusion matrix. The number of test sample points was determined based on the Estok-Navitte-Cowan formula, calculated proportionally for each land cover class. Accuracy testing was conducted by comparing image interpretation results with field-observed reference points. Reference points were determined using the stratified random sampling method. Overall accuracy and the Kappa coefficient were calculated to evaluate the quality of the classification results. The acceptable accuracy for image interpretation in this study was set at 85% or higher. Additionally, class-specific accuracies were calculated, including producer’s accuracy, user’s accuracy, and overall accuracy (Zhou et al., 2011).

Analysis of land-cover projections using the Cellular Automata Model with LanduseSim software, which predicts land use and allows users to control all spatial simulation procedures, such as growth targets and other driving factors (Xu et al., 2022). The driving factors consist of four variables: proximity to primary and secondary roads, proximity to settlements, and proximity to rivers; meanwhile, the inhibiting factors include protected forest areas and the district’s spatial planning (RTRW) patterns (Putra and Rudiarto, 2018).

### Cellular automata-based land-use projection parameters

The 2045 land-use projection was generated in LanduseSim using a Moore neighbourhood (3 × 3 kernel) transition rule over 500 iterations distributed across 20 simulation timesteps, projecting from the 2025 base map to 2045 under a business-as-usual scenario (no policy

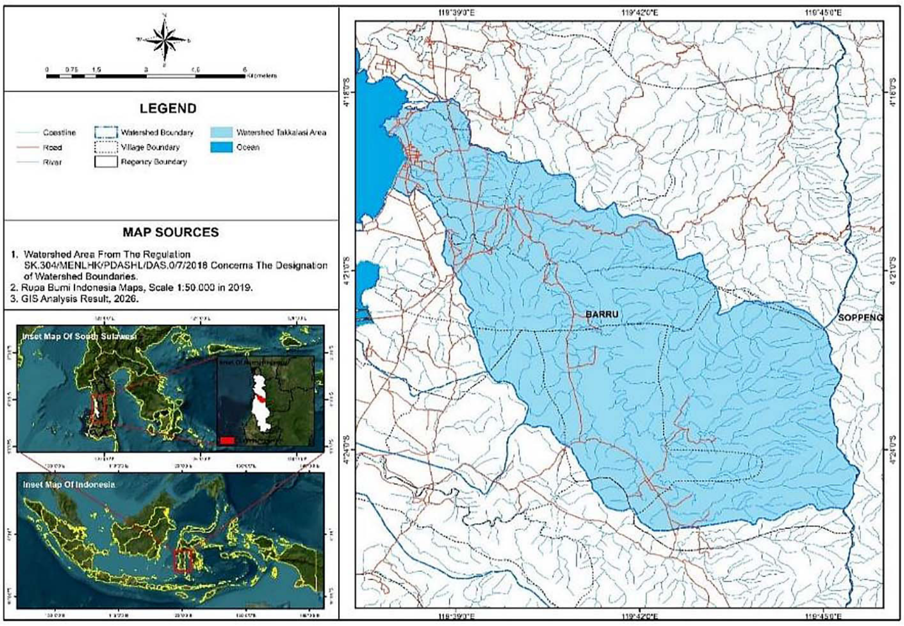


**Figure 1.** Research location map

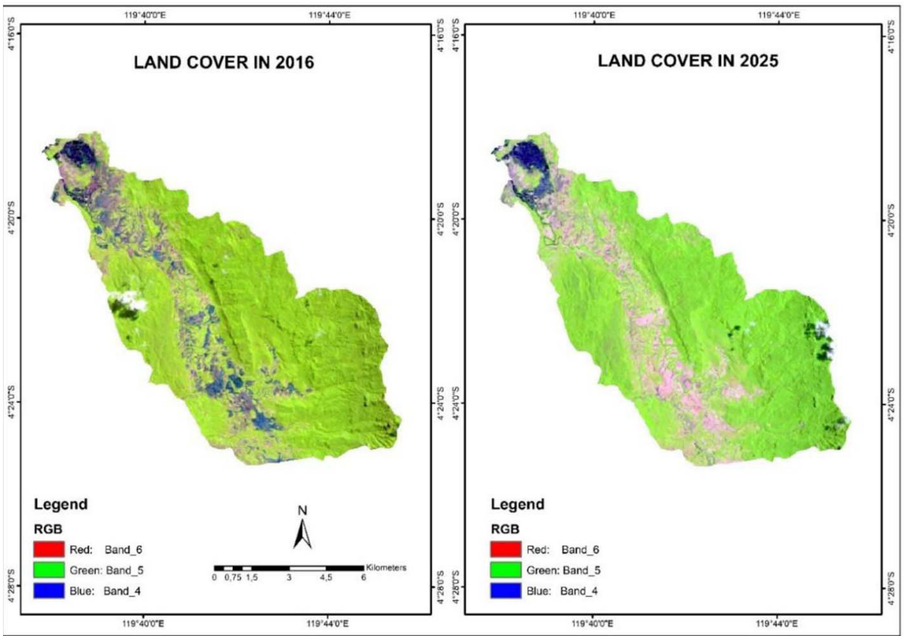


**Figure 2.** Preparation of spatial data for land cover analysis: a) Landsat 8 imagery from 2016; b) Landsat 8 imagery from 2025

intervention). Settlement was designated as the sole growth-target class, constrained by two restriction layers: the gazetted protected-forest boundary and the district spatial-plan (RTRW) pattern layer, both supplied as GIS input (Supplementary File S2). Cell transition probability was driven by three weighted proximity factors distance to existing settlement (weight 0.45), distance to the primary road network (weight 0.30), and distance to the secondary road network (weight 0.25) derived from the relative influence of accessibility on historical (2016–2025) settlement expansion in the watershed. The complete parameter set, including the simulated area of each land-cover class at five-year output steps (2029, 2033, 2037, 2041, 2045), is documented in Supplementary File S1 and the accompanying parameter workbook.

The original LanduseSim project file was not retained after the simulation run; consequently, the model configuration, transition rule, driving-factor weights, constraint layers, and full simulated output trajectory are provided as supplementary documentation in place of the project file to support independent reconstruction and reproducibility of the projection. An internal consistency check, obtained by cross-tabulating the classified 2025 map against the simulated 2045 map at a common 10 m grid, yielded an overall agreement of 94.36% and a Kappa coefficient of 0.91, indicating that the simulated transition pattern is internally coherent with the 2025 baseline. This is a projection-consistency check and should not be interpreted as an independent field-based accuracy assessment of the (not yet observed) 2045 land cover.

## Surface drought susceptibility assessment using frequency ratio

### *The land surface temperature approach for drought identification*

Land surface temperature (LST) is used in research as a primary approach for identifying droughts and as a biophysical surface indicator that reflects thermal responses to land use differences. LST represents the actual land surface temperature recorded by satellites, making it highly sensitive to changes in vegetation cover, soil moisture levels, and the prevalence of impervious surfaces in built-up areas. LST data were obtained from Band 10 (Thermal Infrared Sensor/TIRS) of Landsat 8 imagery from 2016 to 2025 and analyzed using the formula proposed by Avdan and Jovanovska (2016). Images were selected from the driest months of each year to optimally represent thermal stress and surface moisture conditions for drought analysis. The processed LST results are presented in raster format in degrees Celsius and classified based on the criteria Liviona et al.,(2020) into four classes : <20 °C (very low), 20–25 °C (low), 25–30 °C (moderate), and 30–35 °C (high). This classification was then further grouped into two main categories: non-drought (<20 °C and 20–25 °C) and drought (25–30 °C and 30–35 °C). The raster results were then converted to vector data, with only the areas classified as drought extracted and overlaid with subsequent-year data, yielding a single dataset showing the distribution of drought events throughout the study period.

Because LST characterizes surface thermal and vegetation-water-stress conditions rather than atmospheric precipitation deficit, drought as assessed in this study is more precisely termed a thermal (surface) drought susceptibility assessment rather than a meteorological drought assessment. Independent meteorological drought indices such as the standardized precipitation index (SPI), the standardized precipitation evapotranspiration index (SPEI), or the palmer drought severity index (PDSI) were not incorporated, because this study was scoped to satellite-derived surface drought characteristics; this scope is stated explicitly as a limitation of the present assessment.

### *Collection of drought factor data*

The variables used in this study include rainfall, soil texture, land cover, building density, hotspot area, vegetation density, slope gradient, and distance from the river. The selection of analysis parameters was based on scientific reference studies and adjusted according to the availability of existing data (Thamrin et al., 2025). All of these factors will be used as input variables in calculating the drought vulnerability index for the study area.

Daily rainfall data were obtained from the NASA/POWERCERES/MER-RA-2 satellite via the Data Access Viewer website. The data were then processed using Microsoft Excel to calculate the average annual rainfall. The processed tabular data were integrated into the station point shapefile in GIS software using the "Join" and "Relate" features. Rainfall maps were created using the inverse distance weighting (IDW) interpolation method and then classified according to rainfall classes defined by Riajaya et al., (2024), which consist of: 1.500–200 mm/year, 2.000–2.500 mm/year, 2.500–3.000 mm/year, and >3.000 mm/year.

Slope data for the study area were obtained from digital elevation model (DEM) data using the Slope tool in GIS software. This process produced a slope raster, which was subsequently reclassified into five slope classes in accordance with the study by Utama and Indriani (2021), namely 0–8% (flat), 8–15% (gentle), 15–25% (moderately steep), 25–45% (steep), and >45% (very steep). The selection of the slope variable is based on its influence on surface runoff rates, rainwater infiltration, and soil moisture retention, with steeper slopes generally exhibiting greater drought susceptibility due to rapid drainage (Defwaldi et al., 2024).

Data on distance from rivers were obtained from the Indonesian Topographic Map produced by the National Geospatial Information Agency, in the form of river network data, and analyzed using the Euclidean distance tool in GIS software. These data represent the level of spatial proximity or linear range of the study area to major surface water sources. Areas close to the river network are more drought-resilient due to greater potential for groundwater retention and better water accessibility, whereas areas far from water bodies are more vulnerable to drought risks due to a lack of hydrological influence (Faiz et al., 2025). The resulting distance raster was then reclassified into four classes based on the criteria Prasetyo et al., (2018), namely 0–100 m, 100–250 m, 250–500 m, and >500 m.

Soil texture data were obtained from the Landsystem Regional Physical Planning Programme for Transmigration (RePPProt) soil map published by the National Survey and Mapping Coordination Agency in 1987 at a scale of 1:2,500,000. These maps provide soil texture information across three depth layers: the 0–30 cm top layer, the 30–60 cm (middle layer), and the 60–90 cm (bottom layer). These three layers are identified separately to understand the vertical variations in soil physical properties that influence infiltration capacity, water retention, and the potential for subsurface drought. Although historical in nature, RePPProT data remain relevant for spatial drought analysis to this day because they reflect relatively stable basic soil characteristics on a decadal timescale (Sulaeman et al., 2013).

Building density data were obtained using Landsat 8 satellite imagery via the normalized difference built-up index (NDBI) approach. This analysis was conducted using GIS software via the Raster Calculator tool in ArcToolbox. According to Ridwan et al. (2021), the NDBI approach is capable of characterizing the intensity of built-up areas, including both residential and industrial zones. The results of the NDBI analysis range from -1 to 1, with negative values indicating undeveloped areas (vegetation or water bodies) and positive values indicating built-up areas. This study adopted the equation developed by Zha et al.,(2003), namely:

$$\text{NDBI} = \frac{(\rho SWIR1 - \rho NIR)}{(\rho SWIR1 + \rho NIR)} \tag{1}$$

where: $\rho$ *SWIR*1 – Band 6; $\rho$ *NIR* – Band 5.

Vegetation density data were analyzed using the normalized difference vegetation index (NDVI) approach, derived from Landsat 8 Bands 5 (NIR) and 4 (red). NDVI is one of the most commonly used vegetation indices to describe vegetation density and health. Vegetation density has a positive correlation with water retention capacity in a given area(Kang et al., 2013). Spatially, areas with high vegetation density and optimal water absorption capacity are indicated by high NDVI values. Conversely, a decrease in NDVI values indicates areas affected by drought, characterized by low vegetation density and a reduced surface water absorption capacity (Karnieli et al., 2010). NDVI values range from -1 to 1. The formula used to calculate the NDVI value is:

$$NDVI = \frac{(\rho NIR - \rho Red)}{(\rho NIR + \rho Red)} \tag{2}$$

where: $\rho$ NIR – Band 5 (Near-Infrared);
$\rho RED$ – Band 4.

Hotspot distribution data were obtained from the Visible Infrared Imaging Radiometer Suite (VIIRS) sensor on NASA's Suomi National Polar-orbiting Partnership (S-NPP) satellite. The data were downloaded in shapefile (.shp) format for the study period via NASA's Fire Information for Resource Management System (FIRMS) at: https://firms.modaps.eosdis.nasa.gov/. Spatial analysis of hotspot distribution was conducted through several steps using GIS software. The process began by integrating the positions of adjacent hotspots using the Integrate tool, followed by calculating the cumulative number of nearest points through the Collect Events step. Next, a spatial cluster analysis was performed using the Spatial Autocorrelation method (Moran's I) to identify data distribution patterns, which were then mapped in greater detail using the Getis-Ord Gi* hotspot analysis. The z-scores generated from this process were then interpolated using the IDW tool to create a continuous surface representing the distribution of hotspots. In the final stage, the interpolation results were manually reclassified into three vulnerability levels based on z-score values: low (<1), moderate (1–2), and high (>2).

The land cover data used as a variable in the drought factor analysis is based on a dataset consistent with previous land cover change analyses, namely Landsat 8 imagery from 2025. This integration aims to maintain consistency among the spatial variables used in modeling. By using the same multitemporal data sources, the interpretation of land surface characteristics can be analyzed linearly, thereby minimizing spatial bias associated with existing land cover types (Figure 3) (Panuju et al., 2020).

*Drought mapping analysis using the frequency ratio method and the drought susceptibility index*

The frequency ratio is a widely used bivariate analysis (BSA) technique for assessing the spatial relationship between drought events and their contributing factors. This method assigns a weight to each variable's subclass based on the probability of a drought event occurring (Abdekareem et al., 2023). In this analysis, the drought identification data and all processed drought-causing factors were converted into raster format. Drought identification data were coded as 0 for non-drought areas and 1 for drought-affected areas. Additionally, data for each drought-causing factor were assigned sequential numerical codes corresponding to the number of classes in each variable. It is important to note that FR quantifies the statistical spatial association between each factor class and drought occurrence; it does not establish a causal relationship between the two, and the results should be interpreted accordingly.

Next, the raster data for drought identification was converted to a point vector format using the "Raster to Point" tool, and the raster data for drought-causing factors was extracted using the "Extract Multivalue to Point" tool in the GIS software. In this process, the drought data were used as point features, and all raster data on contributing factors served as raster inputs. The FR was calculated by comparing the proportion of drought occurrences to the area in each class of drought-causing factors, using the following formula:

$$FR = \frac{PxcL\,\dfrac{nm}{\sum PnxL}}{Pixel\,\dfrac{nm}{\sum Pnx}} \qquad (3)$$

where: *Pxcl* – number of pixels with drought occurrences within class n of parameter m (nm), *Pixel* – the number of pixels in class n of parameter m (nm), ∑*Pnxl* – total number of pixels for parameter m, ∑*Pnx* – total number of pixels in the area.

This process yields a FR value for each class across each drought factor. An FR value greater than 1.0 indicates a strong positive relationship between that factor class and the occurrence of drought, while an FR value less than

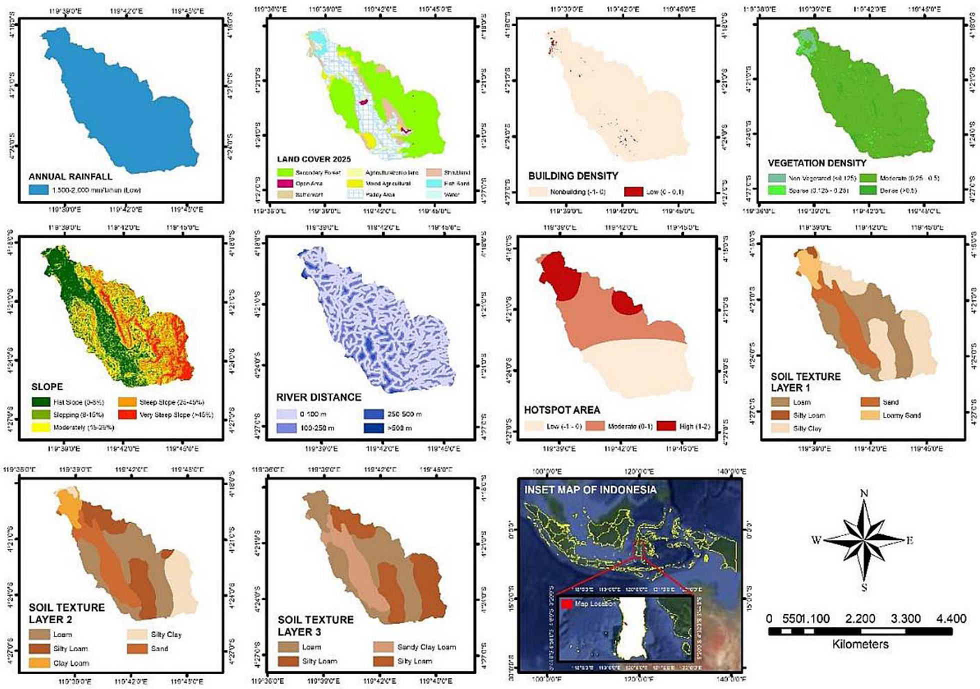


**Figure 3.** Data collection for drought factors: a) annual precipitation; b) land cover in 2025; c) NDBI; d) NDVI; e) slope; f) distance to a river; g) hotspot area; h) soil texture layer 1; i) soil texture layer 2; j) soil texture layer 3

1.0 indicates a weak relationship. The FR values for all variables are then spatially summed to construct a drought susceptibility index (DSI) map. This index is calculated using the following formula:

$$DSI: Fr_1 + Fr_2 + ... Fr_n \tag{4}$$

where: $Fr1$, $Fr2$,...: raster maps of frequency ratios for the factors.

In the final stage, the DSI raster was classified into five surface drought susceptibility categories very low, low, moderate, high, and very high using the Natural Break (Jenks) algorithm in GIS software. This method was chosen for its ability to optimally group data based on the natural distribution patterns of DSI values, thereby producing more representative class boundaries and minimizing variation within each class.

### Model validation

In the study Nguyen et al., (2021) drought event data were divided according to a 70:30 validation ratio to assess the effectiveness of the FR method in estimating drought probability. 70% of the data was allocated to training to evaluate model performance, and 30% was set aside for validation to assess the model's predictive accuracy. This validation demonstrates the FR method ability to predicts drought. The validation results show the prediction accuracy based on the AUC through ROC analysis using the Statistical Program for the Social Sciences (SPSS). The AUC equation is as follows.

$$AUC = \sum \mathrm{TP} + \sum \frac{TN}{P + N} \tag{5}$$

where: $TP$ – true positive, $TN$ – true negative, $P$ – total number of droughts, $N$ – total number of non-drought events.

Areas with values close to 1 indicate successful predictions by the method, while values below 0.5 indicate low accuracy. On the ROC curve, the x-axis represents specificity the probability of incorrectly predicting a non-drought location and the y-axis represents sensitivity the success rate in predicting drought locations. The AUC classification in the studies Balamurugan et al. (2017) and Naghibi et al. (2015) is as follows: perfect (0.9–1.0), very good (0.8–0.9), good (0.7–0.8), average (0.6–0.7), and poor (0.5–0.6).

## RESULTS AND DISCUSSION

### Historical land cover changes (2016–2025)

The interpretation of satellite imagery in the Takkalasi Watershed yielded nine land cover classes: secondary forest, open area, settlements, agricultural/crop land, mixed agriculture, paddy area, shrubland, fish bonds and water. Verification and validation of the classification results were conducted differently across periods. For 2016, validation was performed by comparing the classification results with high-resolution imagery from Google Earth Pro as reference data. Meanwhile, validation for 2025 was conducted through direct field surveys (Ramadhan et al., 2026; Islami et al., 2022).

The accuracy test results show 93.60% overall accuracy in 2016 and 94.19% in 2025. The Kappa coefficients obtained were 92.26% (2016) and 92.22% (2025). These accuracy values indicate a very high level of precision, far exceeding the generally accepted minimum threshold of 80% for both overall accuracy and the Kappa coefficient (McCombs et al., 2016). This high accuracy demonstrates the reliability of the land cover classification results, which can be used for historical change analysis and for input inti land cover projection modelling (Vahid and Aly, 2025).

Based on Table 1, land cover conditions in the Takkalasi Watershed in 2016 and 2021 were dominated by secondary forest, although it decreased by 40.44 Ha. Over the ten-year period, there were significant changes in land cover dynamics, marked by increases and decreases in the area of several land cover classes. The most significant land cover change was an increase in the area of paddy area by 356.52 Ha, with an annual growth rate of 39.61 Ha/year. This increase was followed by expansions in open area (+48.72 Ha) and settlements (+44.93 Ha). Conversely, the largest decreases in area occurred in the agricultural/crop land class (-191.65 ha) and the Shrubland class (-163.57 ha).

These findings indicate a trend toward intensification of wet agriculture and the conversion of agricultural/crop land class and shrubland into productive land and built-up areas. The annual rate of land cover change in the Takkalasi Watershed shows the most significant increase in the rice paddy class and a substantial decrease in dryland agriculture and scrubland. Although the expansion of rice paddies may increase food

**Table 1.** Land cover changes in 2016 and 2025 in the Takkalasi Watershed

| Land cover | Area in 2016 | | Area in 2025 | | Area change (2016–2025) | |
|---|---|---|---|---|---|---|
| | Ha | % | ha | % | Ha | Ha/Year |
| Secondary forest | 4,952.17 | 53.15 | 4,911.73 | 52.71 | -40.44 | -4.49 |
| Open area | 11.20 | 0.12 | 59.92 | 0.64 | 48.72 | 5.41 |
| Settlement | 230.99 | 2.48 | 275.92 | 2.96 | 44.93 | 4.99 |
| Agricultural/crop land | 374.65 | 4.02 | 183.00 | 1.96 | -191.65 | -21.29 |
| Mixed agriculture/Agroforestry | 566.06 | 6.08 | 507.28 | 5.44 | -58.78 | -6.53 |
| Paddy area | 1,984.22 | 21.30 | 2,340.74 | 25.12 | 356.52 | 39.61 |
| Shrubland | 885.07 | 9.50 | 721.10 | 7.74 | -163.97 | -18.22 |
| Fish bond | 255.05 | 2.74 | 259.50 | 2.79 | 4.45 | 0.49 |
| Water | 58.18 | 0.62 | 58.40 | 0.63 | 0.22 | 0.02 |
| Total area | 9,317.57 | 100 | 9,317.57 | 100 | | |

production, the reduction in shrubland and natural forests may decrease water retention and infiltration in the upstream region (Anwar et al., 2011). This could potentially exacerbate vulnerability to drought in the future. These changes align with the land-conversion patterns commonly observed in many watersheds in South Sulawesi, driven by to anthropogenic pressures and the need for agricultural land (Marwah, 2014).

The increase in rice paddies and settlements, offset by a decline in shrubland and dryland agriculture, reflects a landscape transformation from a subsistence agricultural system toward a more intensive agricultural system and population urbanization in the Takkalasi watershed (Parera, 2024). These changes not only alter the landscape structure but also have the potential to affect the region's hydrological balance (Sujarwo et al., 2023). The decline in natural vegetation, such as shrubs and thickets that act as buffers for rainwater infiltration, can accelerate surface runoff and groundwater recharge (Yadav, 2023). Therefore, the dynamics of land cover change over the past decade serve as a crucial foundation for understanding the increased risk of drought in the Takkalasi Watershed.

## Projected land cover changes in 2045

An internal consistency assessment of the 2045 land cover projection, obtained by cross-tabulating the classified 2025 base map against the simulated 2045 map, indicated strong agreement between the simulated transition pattern and the 2025 baseline, with an Overall Accuracy of 92.69% and a Kappa coefficient of 88.93%. Because the 2045 land cover has not yet been observed, these values should be interpreted as measures of internal model consistency relative to the 2025 starting condition, rather than as a field-validated accuracy assessment of the projection itself. Nonetheless, values well above the commonly cited acceptability thresholds of 85% for Overall Accuracy and 80% for Kappa (Kundu et al., 2025) indicate that the simulated land-use transition process is internally coherent, providing a reasonable basis for exploring plausible future landscape trajectories and their implications for surface drought susceptibility in the Takkalasi Watershed.

Based on a Cellular Automata model simulation using the LanduseSim software, the projected changes in land cover in the Takkalasi Watershed, shown in Table 2, indicate a fairly significant trend compared to conditions in 2025. The most dominant change is a significant increase in settlement area, reaching 641.28 Ha an average growth of 32.06 Ha per year. Conversely, there was a decrease in the area of several agricultural land classes, particularly paddy fields (-515.61 ha) and agricultural/crop land (63.92 ha). Similarly, secondary dryland forests and shrublands also experienced a decrease in area, albeit with smaller changes.

The visualization of land cover changes in the projection years shown in Figure 4a displays a bar chart of area by land cover class, revealing that the settlement area is the only land cover class experiencing positive growth. In the study Salvacion (2021), it is stated that the expansion of built-up areas replacing agricultural land and natural vegetation is the dominant pattern of land cover change in developing tropical regions, with

**Table 2.** Projected changes in land cover for the year 2045 in the Takkalasi Watershed

| Land cover | Area in 2025 | | Area in 2045 | | Area change (2025–2045) | |
|---|---|---|---|---|---|---|
| | Ha | % | ha | % | Ha | Ha/Year |
| Secondary forest | 4,911.73 | 52.71 | 4,908.40 | 52.68 | -3.33 | -0.17 |
| Open area | 59.92 | 0.64 | 57.80 | 0.62 | -2.12 | -0.11 |
| Settlement | 275.92 | 2.96 | 917.20 | 9.84 | 641.28 | 32.06 |
| Agricultural/crop land | 183.00 | 1.96 | 119.08 | 1.28 | -63.92 | -3.20 |
| Mixed agriculture/Agroforestry | 507.28 | 5.44 | 484.33 | 5.20 | -22.95 | -1.15 |
| Paddy area | 2,340.74 | 25.12 | 1,825.13 | 19.59 | -515.61 | -25.78 |
| Shrubland | 721.10 | 7.74 | 687.11 | 7.37 | -33.99 | -1.70 |
| Fish bond | 259.50 | 2.79 | 259.48 | 2.78 | -0.01 | 0.00 |
| Water | 58.40 | 0.63 | 59.06 | 0.63 | 0.66 | 0.03 |
| Total area | 9,317.57 | 100 | 9,317.57 | 100 | | |

serious implications for the water balance. Meanwhile, the settlement expansion trend projected in this study shows a progressive and consistent growth pattern throughout the simulation period. Based on Figure 4b, the cumulative growth projection for the settlement area shows a linear increase from 275.92 ha in 2025 to 917.20 ha in 2045, with an average increase of 128.26 ha per five-year interval. This growth rate indicates a relatively stable acceleration, with the increase in area over each five-year interval ranging from 104.30 ha to 145.83 ha, suggesting that the pressure for land conversion to built-up areas shows no signs of slowing. Beyond the change in area itself, this settlement expansion carries direct ecological consequences: the progressive replacement of vegetated and agricultural surfaces with impervious built-up land is expected to reduce infiltration capacity and evapotranspiration, and to elevate surface temperatures in the affected zones, thereby reinforcing conditions conducive to surface drought susceptibility.

These land-cover changes are projected to occur primarily in the lower and middle reaches of the Takkalasi watershed, as shown in Figure 5. These areas are expected to be growth centers due to strong driving factors in the model, including proximity to the road network, high accessibility, and proximity to existing settlement centers. Supporting factors such as relatively flat topography and proximity to water bodies also accelerate the conversion of agricultural land into built-up areas (Mitsuda and Ito, 2011). The results of this simulation depict a "Business as Usual" scenario, in which trends of urbanization and the conversion of agricultural land into residential areas continue unabated without strong policy intervention (Wu et al., 2011). Massive increases in residential development in the middle and lower reaches of the watershed could increase pressure on water resources and heighten susceptibility to future surface drought conditions, given that built-up land has low water infiltration and retention capacity (Muhammad et al., 2020).

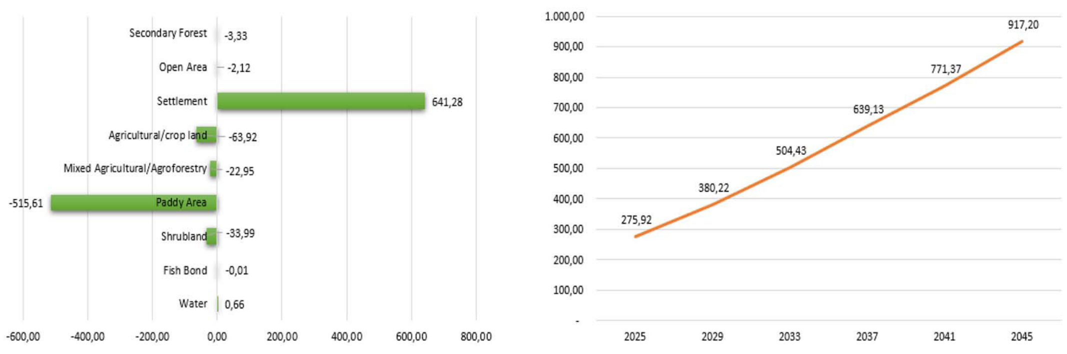


**Figure 4.** Graph of land cover changes: (a) change in area by class (2025 → 2045) (b) projected settlement growth (5-year iteration)

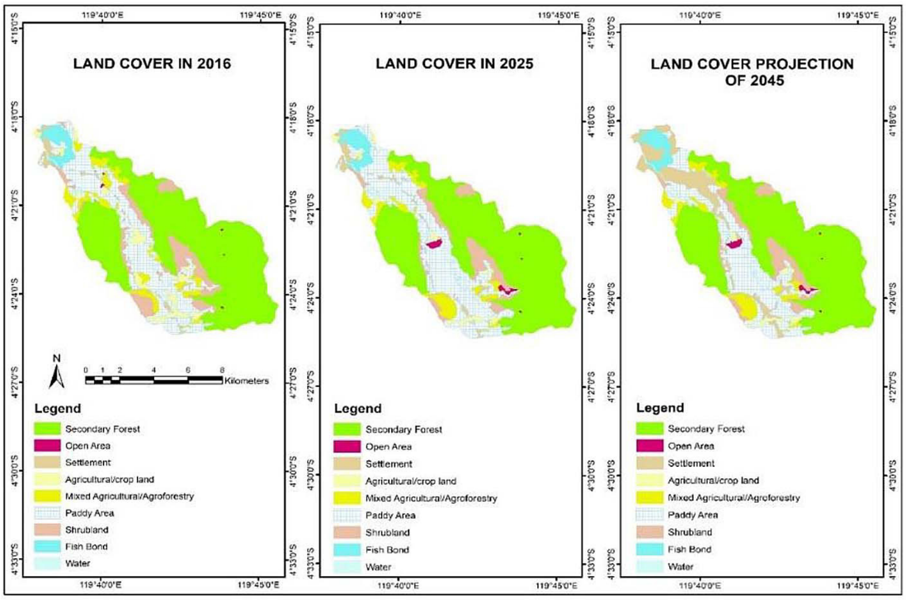


**Figure 5.** Spatial land cover map for 2016–2025 and projections for 2045 in the Takkalasi Watershed

## Analysis of land surface temperature in the Takkalasi Watershed

Analysis of land surface temperature (LST) from Landsat 8 OLI/TIRS imagery (Figure 6) reveals varying results across the Takkalasi watershed during the study period. The highest land surface temperature was recorded in 2019, reaching 41 °C, followed by 2023 with a maximum temperature of 37 °C and 2016 at 34 °C. This increase in extreme temperatures was driven by a strong El Niño phenomenon. This is supported by studies by Thamrin et al. (2025) and Yuniasih et al. (2024), which report that Indonesia experienced El Niño events during that period. A drastic increase in surface temperature can accelerate groundwater evaporation and reduce soil surface moisture, thereby exacerbating drought, especially in areas with sparse vegetation (Cassardo, 2014).

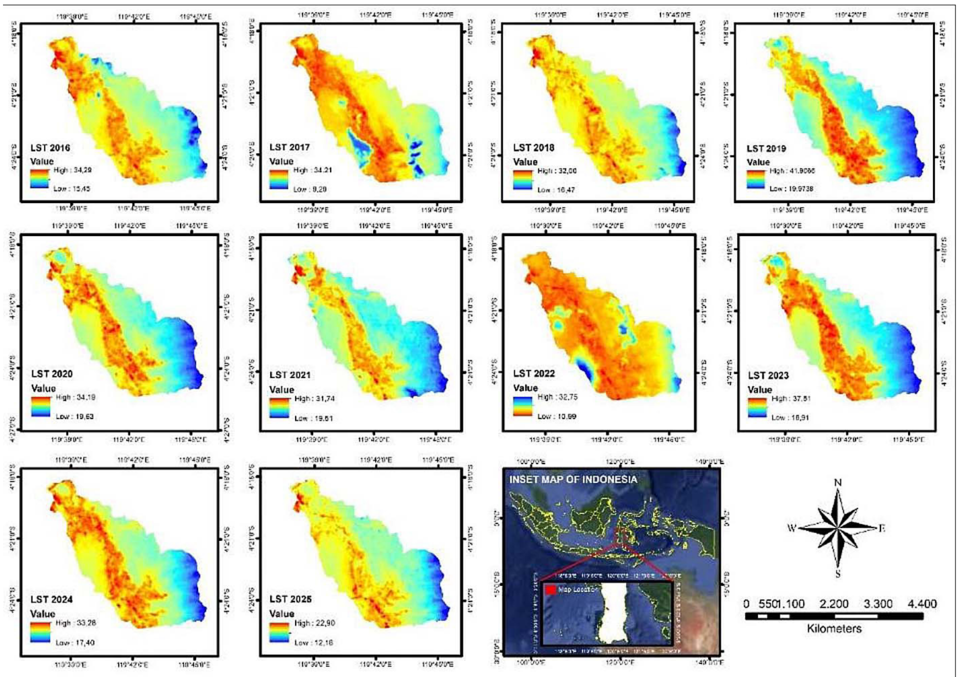


**Figure 6.** LST map of the Takkalasi Watershed from 2016 to 2025

## Surface drought susceptibility assessment using the FR model

The FR values presented in Table 3 were obtained through a bivariate statistical approach based on Equation 3. The FR values are not necessarily a direct result of the spatial analysis process, but are calculated from the ratio of the proportion of drought occurrences to the area of each factor subclass. Specifically, the number of pixels experiencing drought in each factor class (PxCL) was obtained through the "Extract Multi-Values to Point" process, while the number of pixels in each factor class (PnXL) was calculated using raster statistics. These two values were then substituted into the FR equation to produce vulnerability weights for each factor.

Based on the analysis results, building density (FR = 1.82), residential land cover (FR = 1.81), and rice paddies (FR = 1.78) show the strongest spatial association with surface drought susceptibility in the Takkalasi Watershed. These patterns are consistent with urban hydrology theory, which indicates that an increase in built-up areas and building density is associated with a reduction in rainwater infiltration capacity and an increase in surface runoff, thereby reducing groundwater recharge and being linked to greater surface drought susceptibility (Weng, 2012). Several studies in tropical regions have also shown that high-density residential areas tend to have higher surface temperatures and lower water retention capacity, a combination associated with greater water deficits during the dry season (Marcotullio et al., 2021).

Meanwhile, rice field intensification is also strongly associated with higher surface drought susceptibility. Although rice fields are irrigated, converting land from natural vegetation to monoculture rice fields can reduce biodiversity and overall groundwater storage capacity (Azadi et al., 2018). Previous research in Southeast Asia has shown that the expansion of wet agricultural land, if not balanced by water-conservation practices, is associated with greater long-term hydrological susceptibility through increased evapotranspiration and decreased natural vegetation cover (Dimyati et al., 2024).

The results of the drought susceptibility index (DSI) calculation indicate that drought susceptibility in the Takkalasi watershed is distributed heterogeneously. Based on Table 4, areas with very low and low susceptibility levels dominate the watershed, extending from the upper to the middle reaches, accounting for 26.13% and 26.03%, respectively. Meanwhile, overall, approximately 28.63% of the watershed area falls into the high to very high susceptibility categories. The DSI distribution map in Figure 7 shows that areas with high and very high susceptibility are concentrated in the middle to lower reaches of the Takkalasi watershed. This spatial pattern shows a strong association with the factors most strongly linked to drought namely, building density, settlement expansion, and the dominance of agricultural land in relatively flat areas (Murthy et al., 2015). In contrast, the upstream areas of the watershed, which are still dominated by secondary dryland forests and shrublands, tend to exhibit low to very low susceptibility levels (Vogt et al., 2016).

These findings indicate that although most of the Takkalasi watershed remains classified as having low to very low susceptibility, the presence of areas with high and very high susceptibility in the middle to lower reaches warrants special attention. These areas have the potential to experience more severe water deficits during the dry season, reflecting a susceptibility pattern characteristic of watersheds in tropical regions under high anthropogenic pressure (Angeluccetti et al., 2014). Previous research has shown that areas with high pressure are typically concentrated in the middle and lower reaches of river basins due to the cumulative impacts of land conversion, increased surface impermeability, and reduced infiltration capacity (Huang et al., 2016). This situation aligns with the theory that, although most of the region remains relatively safe, the presence of high-susceptibility hotspots can become critical points that threaten the overall hydrological resilience if not properly managed (Giri et al., 2018).

## Model validation

The surface drought susceptibility model was validated using ROC curve analysis by comparing DSI raster values at drought and non-drought sample points, which were classified into a training dataset comprising 70% and validation dataset comprising 30% of the total sample points. The evaluation results show that the AUC (area under the curve) for the Success Rate model was 0.807, while that for the Prediction Rate model was 0.7272. Based on the model performance classification proposed by Balamurugan et al. (2017), the AUC value for the Success Rate model is categorized as "good," while the AUC value for the

**Table 3.** FR values of drought-causing factors

| Factor | Factor class | PxcL | % PxCL | PnXL | % PnXL | FR |
|---|---|---|---|---|---|---|
| Land cover | Secondary forest | 7.409 | 18.28 | 54.561 | 52.70 | 0.35 |
| | Paddy area | 18.586 | 45.85 | 26.634 | 25.72 | 1.78 |
| | Shrubland | 5.191 | 12.81 | 8003 | 7.73 | 1.66 |
| | Settlement | 2.178 | 5.37 | 3.068 | 2.96 | 1.81 |
| | Agricultural/crop land | 1.392 | 3.43 | 2.039 | 1.97 | 1.74 |
| | Mixed agriculture/Agroforestry | 3.905 | 9.63 | 5.661 | 5.47 | 1.76 |
| | Fish bond | 1.424 | 3.51 | 2.886 | 2.79 | 1.26 |
| | Open area | 14 | 0.03 | 46 | 0.04 | 0.78 |
| | Water | 436 | 1.08 | 638 | 0.62 | 1.75 |
| Soil texture L1 | Loam | 10.983 | 27.10 | 37281 | 36.01 | 0.75 |
| | Silty loam | 10.598 | 26.15 | 37.993 | 36.70 | 0.71 |
| | Silty clay | 4106 | 10.13 | 6687 | 6.46 | 1.57 |
| | Sand | 14.133 | 34.87 | 20.388 | 19.69 | 1.77 |
| | Loamy sand | 715 | 1.76 | 1187 | 1.15 | 1.54 |
| Soil texture L2 | Loam | 715 | 1.76 | 16.574 | 16.01 | 0.11 |
| | Silty loam | 10.983 | 27.10 | 21.894 | 21.15 | 1.28 |
| | Clay loam | 10.598 | 26.15 | 37.993 | 36.70 | 0.71 |
| | Silty clay | 4106 | 10.13 | 6687 | 6.46 | 1.57 |
| | Sand | 14.133 | 34.87 | 20.388 | 19.69 | 1.77 |
| Soil texture L3 | Loam | 0 | 0.00 | 15.387 | 14.86 | 0.00 |
| | Silty loam | 10.983 | 27.10 | 21.894 | 21.15 | 1.28 |
| | Sandy clay loam | 15.419 | 38.04 | 45.867 | 44.30 | 0.86 |
| | Silty loam | 14.133 | 34.87 | 20.388 | 19.69 | 1.77 |
| Rainfall | 1,500–2,000 mm/year | 40.535 | 100.00 | 103.536 | 100.00 | 1.00 |
| Slope class | 0–8% | 16936 | 42 | 27.648 | 27 | 1.56 |
| | 8–15% | 9.633 | 24 | 18.874 | 18 | 1.30 |
| | 15–25% | 7.416 | 18 | 20.596 | 20 | 0.92 |
| | 25–45% | 5372 | 13 | 24.612 | 24 | 0.56 |
| | >45% | 1178 | 3 | 11.806 | 11 | 0.25 |
| Building density | Non-building (-1-0) | 40039 | 98.78 | 102.840 | 99.33 | 0.99 |
| | Rare (0–0.1) | 496 | 1.22 | 696 | 0.67 | 1.82 |
| Vegetation density | Non-vegetation (<0.125) | 1092 | 2.69 | 2.466 | 2.38 | 1.13 |
| | Sparse (0.125–0.25) | 1.403 | 3.46 | 2.621 | 2.53 | 1.37 |
| | Moderate (0.25–0.5) | 35.879 | 88.51 | 93.287 | 90.10 | 0.98 |
| | Dense (>0.5) | 2161 | 5.33 | 5.162 | 4.99 | 1.07 |
| River distance | 0–100 m | 24.526 | 61 | 66.489 | 64 | 0.94 |
| | 100–250 m | 13.723 | 34 | 33.202 | 32 | 1.06 |
| | 250–500 m | 2220 | 5 | 3.749 | 4 | 1.51 |
| | >500 m | 66 | 0 | 96 | 0 | 1.76 |
| Hotspot | Low (-1-0) | 18.730 | 46.2 | 45.735 | 44.17 | 1.05 |
| | Moderate (0–1) | 13.904 | 34.3 | 41.614 | 40.19 | 0.85 |
| | High (1-2) | 7901 | 19.5 | 16.187 | 15.63 | 1.25 |

Prediction Rate model falls into the "adequate" category. Both values exceed the minimum threshold required for a model to be considered statistically valid, namely AUC > 0.70; thus, the Frequency Ratio (FR) model developed in this study is assessed as having acceptable internal discriminatory performance to distinguish drought-prone areas from non-drought-prone areas.

**Table 4.** Surface drought susceptibility classes based on DSI values in the Takkalasi Watershed

| DSI | Vulnerability categories | Number of pixels | Area | |
|---|---|---|---|---|
| | | | (Ha) | (%) |
| 5.62–7.84 | Very low | 27,095 | 2,434.28 | 26.13 |
| 7.84–9.89 | Low | 26,830 | 2,425.16 | 26.03 |
| 9.89–11.63 | Medium | 19,861 | 1,790.24 | 19.21 |
| 11.63–13.23 | High | 13,741 | 1,221.02 | 13.10 |
| 13.23–16.19 | Very high | 16,009 | 1,446.88 | 15.53 |
| Total | | 103,536 | 9,317.57 | 100 |

It should be noted transparently that both the 70% training subset and the 30% validation subset were drawn by random sampling from the same overall pool of drought/non-drought points for the study area, rather than from spatially independent or externally held-out locations. Because nearby sample points can share similar environmental conditions (spatial autocorrelation), this sampling design may overstate the model's true predictive independence, and the resulting AUC values should be interpreted as measures of internal consistency rather than fully independent external validation. Spatially independent validation strategies, such as spatial block cross-validation or buffered leave-one-out cross-validation, are recommended for future refinements of this modelling framework (Table 5).

The ROC curve visualizations for both datasets show curves that consistently slope upward toward the top-left corner of the graph, away from the reference diagonal line, indicating that that the models have high sensitivity with relatively low false-positive rates. The difference in AUC values between the Success Rate model and the Prediction Rate model is approximately 0.08, indicating that no significant overfitting occurred during the modeling process; thus, the models retain good generalization ability for data not used in the training process (Balamurugan et al., 2017). These results indicate that the selection of conditioning factors for FR modeling reflects a spatial representation proportional to the dynamics of drought in the study area. The lack of substantial differences in AUC values between the training and validation datasets is an indicator of the model's stability and reliability in the context of spatially-based predictive modelling (Figure 8) (Rahmati et al., 2016).

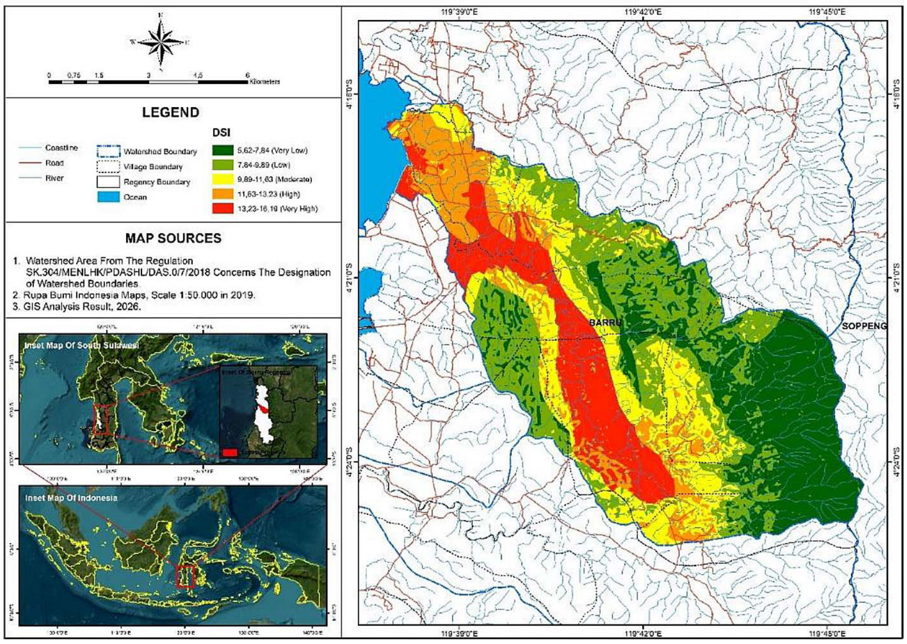


**Figure 7.** Map of surface drought susceptibility indices and classes

**Table 5.** AUC values from ROC validation results for the success rate and prediction accuracy of the FR model for surface drought susceptibility

| AUC | AUC value |
|---|---|
| Model success rate | 0.807 |
| Model prediction rate | 0.727 |

The model validation performance obtained in this study is consistent with the findings of various previous studies that used similar spatial modeling approaches in the context of hydrometeorological disaster susceptibility assessment. Pradhan (2013) in his study on landslide hazard mapping based on the Frequency Ratio method, reported AUC values ranging from 0.72 to 0.85, which are comparable to those obtained in this study. Furthermore, Oh and Pradhan (2011) affirm that an AUC value for the Model Prediction Rate above 0.70 meets the validation criteria for use as a basis for decision-making in spatially-based disaster mitigation efforts. In the field of drought research, Rhee et al. (2010) state that the integrating of remote sensing-based indices, such as DSI into a spatial modeling framework, can significantly improve the accuracy of drought condition representation, particularly when combined with robust statistical validation methods such as ROC-AUC analysis. Beyond methodological benchmarking, these results are also consistent with broader evidence from other tropical watershed studies: Vogt et al. (2016) and Guzha et al. (2018), for instance, similarly report that land-cover conversion in tropical river basins measurably reduces hydrological regulation capacity and elevates drought-related risk, reinforcing the relevance of the present findings beyond the Takkalasi watershed. Thus, the Frequency Ratio model for surface drought susceptibility mapping developed in this study meets the validity standards set in the scientific literature; it can therefore be deemed suitable and reliable as a basis for compiling surface drought susceptibility maps in the study area.

## Integration of land cover dynamics and surface drought susceptibility

The results of integrating land cover dynamics analysis and surface drought susceptibility modeling using the frequency ratio method reveal a strong, systematic relationship between the two variables in the Takkalasi Watershed. Areas experiencing a decline in natural vegetation cover particularly in secondary dryland forests and shrublands and accompanied by an increase in the extent of built-up land and rice fields consistently exhibit higher DSI values, with building density, residential land cover, and rice fields identified as conditioning factors with the highest Frequency Ratio values. Mechanistically, this pattern reflects a coherent ecological pathway: a decline in vegetation cover reduces evapotranspiration and the soil's water-retention capacity, which in turn elevates land surface temperature and reduces moisture availability at the surface, ultimately increasing surface drought susceptibility. This condition is exacerbated by surface temperature anomalies associated with the El Niño phenomenon, which accelerate groundwater evaporation and reduce surface area in regions with low vegetation cover

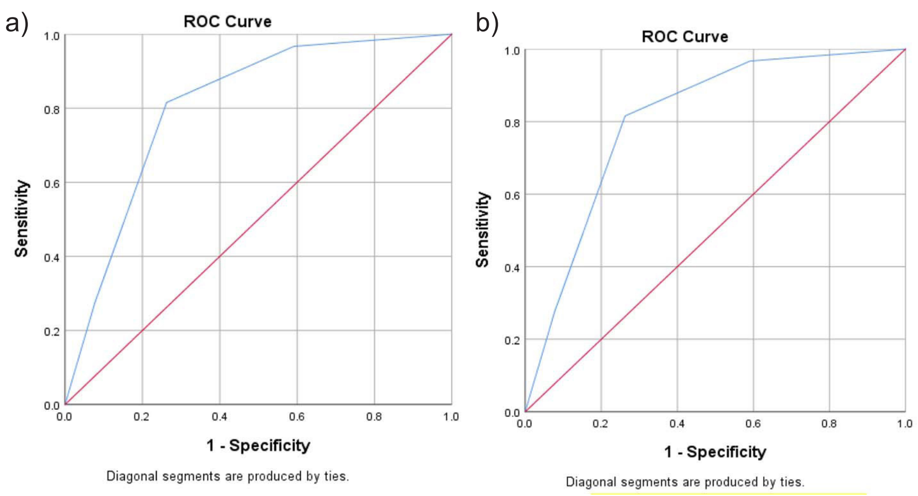


**Figure 8.** ROC curves from the ROC validation results against FR for surface drought susceptibility modeling: (a) model success rate, (b) model prediction rate

(Thamrin et al., 2025). Historically, the decline in the area of dryland agriculture and scrubland has been positively correlated with the expansion of areas with moderate to high susceptibility, while upstream watershed areas still dominated by forest cover consistently exhibit relatively low susceptibility levels, consistent with the findings Guzha et al., (2018) that the conversion of forests and natural vegetation into agricultural land or built-up areas in tropical regions significantly reduces the hydrological regulation functions of watersheds.

Land-cover projections through 2045 using cellular automata simulations further reinforce this relationship, showing that massive settlement expansion, accompanied by a decline in the area of rice paddies and natural vegetation, is predicted to substantially expand areas with high to very high susceptibility in the middle to lower reaches of the watershed, as emphasized by Salvacion (2021), who note that the expansion of impervious areas due to uncontrolled urbanization strongly correlates with increased intensity and duration of hydrological droughts in tropical watersheds. Overall, an integrated approach combining land cover dynamics analysis, Cellular Automata projection simulations, and Frequency Ratio-based susceptibility modeling has yielded a comprehensive spatial understanding of the mechanisms underlying the formation and escalation of surface drought susceptibility in the Takkalasi watershed, thereby making this methodological framework a potentially relevant scientific tool for developing risk-based spatial planning and formulating watershed-level climate change adaptation strategies (Pokhrel et al., 2021).

From an ecological engineering perspective, these findings point to concrete, spatially targeted management interventions capable of moderating future increases in surface drought susceptibility. Priority actions include riparian buffer restoration and forest-cover conservation in the upper and middle reaches to sustain evapotranspiration and baseflow regulation; the promotion of agroforestry systems in transitional zones between forest and agricultural land to maintain partial canopy cover and root-zone water retention; and the incorporation of infiltration-enhancing and green-infrastructure measures (e.g., bioswales, permeable surfaces, and retention ponds) within projected settlement-expansion zones in the middle and lower reaches. Embedding these ecological engineering measures into district spatial planning (RTRW) and watershed management plans could help offset the hydrological consequences of the anthropogenic land-cover change identified in this study.

### Limitations of the study

Several limitations should be acknowledged. First, drought susceptibility in this study was assessed through a thermal (LST-based) proxy rather than through independent meteorological drought indices (e.g., SPI, SPEI, PDSI) or in-situ soil moisture measurements; the resulting susceptibility maps should therefore be interpreted as surface thermal drought susceptibility rather than meteorological or agricultural drought risk in the strict sense. Second, the training and validation samples used in the ROC/AUC evaluation were drawn from the same overall spatial sample pool rather than from an independently held-out spatial subset, which may understate spatial dependency between the two subsets; spatially independent cross-validation is recommended in future work. Third, a formal sensitivity analysis of the cellular automata driving-factor weights (e.g., systematically perturbing the settlement, primary-road, and secondary-road weights by ±20%) was not executed as part of this study; the baseline simulated land-use trajectory (2025–2045) is reported in full in the supplementary material, and a perturbation-based sensitivity design is proposed as a direction for subsequent refinement of the projection model. Fourth, the original LanduseSim project file was not retained after the simulation run; the complete parameter set, driving-factor weights, and simulated output trajectory are provided as supplementary documentation to support reproducibility in place of the project file itself.

## CONCLUSIONS

The study successfully identified the dynamics of land cover change in the Takkalasi Watershed, both historically and prospectively, by integrating multitemporal satellite image analysis with Cellular Automata simulations. The classification results indicate that during the observation period, significant shifts in land cover occurred, characterized by increases in built-up areas, rice fields, and open area and a decrease in natural vegetation, including secondary forests, shrubland and agricultural/crop land. Land cover projections generated through Cellular Automata simulations, which showed a high degree of internal consistency with the 2025 baseline, indicate that these land conversion trends will continue and intensify in the future, with the expansion of residential areas as the dominant change. This overall pattern of land cover transformation reflects increasing anthropogenic pressure on the Takkalasi Watershed ecosystem, which has implications for the balance of its hydrological functions.

Surface drought susceptibility modeling using the Frequency Ratio method, validated via an ROC curve, shows that the developed model possesses acceptable internal discriminatory performance and is statistically adequate for distinguishing between drought-prone and non-drought-prone areas. The spatial distribution of the drought susceptibility index (DSI) shows that areas with high to very high susceptibility are concentrated in the middle to lower reaches of the watershed, which strongly corresponds to areas experiencing the expansion of built-up areas and intensive agriculture. The integration of land cover dynamics and drought susceptibility modelling confirms that the conversion of land cover from natural vegetation types to anthropogenic land is a key determinant shaping and reinforcing the spatial distribution of drought susceptibility in the Takkalasi watershed, both under current conditions and in future projection scenarios. Taken together, these findings indicate that landscape transformation in the Takkalasi watershed functions as an ecological risk pathway that will continue to shape and intensify surface drought susceptibility over time, underscoring the need for proactive, ecologically informed watershed management rather than reactive drought response.

## Acknowledgements

## REFERENCES

1. Abdekareem, M., Abdalla, F., Al-Arifi, N., Bamousa, A. O., El-Baz, F. (2023). Using remote sensing and GIS-based frequency ratio technique for revealing groundwater prospective areas at Wadi Al Hamdh Watershed, Saudi Arabia. *Water (Switzerland)*, 15(6). https://doi.org/10.3390/w15061154
2. Akther, K. R., Sicuro, B., Tafuro, V., Ahmed, S. S., Roy, N. C., Pinna, M. (2026). Influence of climate variability and human activities on carp spawning dynamics in Tanguar haor and the Surma river in Bangladesh. *Discover Environment*, *4*(1). https://doi.org/10.1007/s44274-026-00614-6
3. Angeluccetti, I., Demarchi, A., Perez, F. (2014). Vulnerability analysis for a drought Early Warning System. *EGU General Assembly, 16*(i), 7525.
4. Anwar, M., Pawitan, H., Murtilaksono, K., Jaya, I. (2011). Respons Hidrologi Akibat Deforestasi di DAS Barito Hulu, Kalimantan Tengah Hydrologycal Response Due to Deforestation in Barito Hulu Watershed, Central Kalimantan. *Jurnal Manajemen Hutan Tropika*, *XVII*(3), 119–126. http://jurnal.ipb.ac.id/index.php/jmht/article/view/3985/2724
5. Avdan, U., Jovanovska, G. (2016). Algorithm for Automated Mapping of Land Surface Temperature Using LANDSAT 8 Satellite Data. *Journal of Sensors.*
6. Azadi, H., Keramati, P., Taheri, F., Rafiaani, P., Teklemariam, D., Gebrehiwot, K., Hosseininia, G., Van Passel, S., Lebailly, P., Witlox, F. (2018). Agricultural land conversion: Reviewing drought impacts and coping strategies. *International Journal of Disaster Risk Reduction*, *31*(December 2017), 184–195. https://doi.org/10.1016/j.ijdrr.2018.05.003
7. Balamurugan, G., Seshan, K., Bera, S. (2017). Frequency ratio model for groundwater potential mapping and its sustainable management in cold desert, India. *Journal of King Saud University - Science*, *29*(3), 333–347. https://doi.org/10.1016/j.jksus.2016.08.003
8. Banerjee, R. (2012). Climate change in Indonesia: A glimpse of Riau and East Kalimantan. *Journal of Resources, Energy and Development*, *9*(2), 89–99. https://doi.org/10.3233/red-120097
9. Cassardo, C. (2014). Global warming and water sustainability. *E3S Web of Conferences*, *2*, 1–6. https://doi.org/10.1051/e3sconf/20140202006
10. Chen, D., Elhadj, A., Xu, H., Xu, X., Qiao, Z. (2020). A study on the relationship between land use change and water quality of the Mitidja watershed in Algeria based on GIS and RS. *Sustainability (Switzerland)*, *12*(9). https://doi.org/10.3390/SU12093510
11. Defwaldi, D., Driptufani, D. M., Armi, I., Nasyahardian, N. (2024). Pemetaan Risiko Kekeringan Berbasis Integrasi Kemiringan Lereng dengan Sistem Informasi Geografis. *Jural Riset Rumpun Ilmu Teknik*, *3*(2), 61–70. https://doi.org/10.55606/jurritek.v3i2.6940
12. Dimyati, M., Rustanto, A., Ash Shidiq, I. P., Indratmoko, S., Siswanto, Dimyati, R. D., Nurlambang, T., Zubair, A., Fakhruddin, A., Siddiq, A., Adhanto, D. H., Maulidina, K., Auni, R. (2024). Spatiotemporal relation of satellite-based meteorological to agricultural drought in the downstream Citarum watershed, Indonesia. *Environmental and Sustainability Indicators*, *22*(January), 100339. https://doi.

org/10.1016/j.indic.2024.100339

13. Faiz, M. A., Baig, F., Muneer, S., Zhou, Z., Naz, F. (2025). Response of vegetation resilience to drought across river basins on a global scale. *International Journal of Digital Earth*, *18*(1). https://doi.org/10.1080/17538947.2025.2528661
14. Ghalehteimouri, J. K., Shamsoddini, A., Mousavi, M. N., Binti Che Ros, F., Khedmatzadeh, A. (2022). Predicting spatial and decadal of land use and land cover change using integrated cellular automata Markov chain model based scenarios (2019–2049) Zarriné-Rūd River Basin in Iran. *Environmental Challenges*, *6*(July 2021), 100399. https://doi.org/10.1016/j.envc.2021.100399
15. Giri, S., Qiu, Z., Zhang, Z. (2018). Assessing the impacts of land use on downstream water quality using a hydrologically sensitive area concept. *Journal of Environmental Management*, *213*, 309–319. https://doi.org/10.1016/j.jenvman.2018.02.075
16. Guzha, A. C., Rufino, M. C., Okoth, S., Jacobs, S., Nóbrega, R. L. B. (2018). Impacts of land use and land cover change on surface runoff, discharge and low flows: Evidence from East Africa. *Journal of Hydrology: Regional Studies*, *15*(May 2017), 49–67. https://doi.org/10.1016/j.ejrh.2017.11.005
17. Hakiki, L. K., Achmad, M., Soma, A. S., Amin, U. H. (2026). Prediction of land use changes via the cellular automata-Markov model in East Luwu Regency. *Ecological Engineering and Environmental Technology*, *27*(1), 350–363. https://doi.org/10.12912/27197050/215827
18. Hatta, M. P., Yuni, S. S. (2019). Changes in rainfall and discharge in Saddang Watershed, South Sulawesi, Indonesia. *IOP Conference Series: Earth and Environmental Science*, *235*(1). https://doi.org/10.1088/1755-1315/235/1/012037
19. Huang, X. D., Shi, Z. H., Fang, N. F., Li, X. (2016). Influences of land use change on baseflow in mountainous watersheds. *Forests*, *7*(1). https://doi.org/10.3390/f7010016
20. Islami, F. A., Tarigan, S. D., Wahjunie, E. D., Dasanto, B. D. (2022). Accuracy Assessment of Land Use Change Analysis Using Google Earth in Sadar Watershed Mojokerto Regency. *IOP Conference Series: Earth and Environmental Science*, *950*(1). https://doi.org/10.1088/1755-1315/950/1/012091
21. Kang, L., Shao, Y., Zhang, B., Di, L., Yu, E., Shrestha, R. (2013). Study of the NDVI-precipitation correlation stratified by crop type and soil permeability. *2013 Second International Conference on Agro-Geoinformatics (Agro-Geoinformatics)*, 194–199. https://doi.org/10.1109/Argo-Geoinformatics.2013.6621906
22. Karnieli, A., Agam, N., Pinker, R. T., Anderson, M., Imhoff, M. L., Gutman, G. G., Panov, N., Goldberg, A. (2010). Use of NDVI and land surface temperature for drought assessment: Merits and limitations. *Journal of Climate*, *23*(3), 618–633. https://doi.org/10.1175/2009JCLI2900.1
23. Kundu, S., Rani, A., Kumar, V. (2025). Enhanced Accuracy in Cellular Automata-Markov Chain Model for Land Classification Analysis and Prediction. *Communications on Applied Nonlinear Analysis*. https://api.semanticscholar.org/CorpusID:277404210
24. Li, L., Lan, H., Guo, C., Zhang, Y., Li, Q., Wu, Y. (2017). A modified frequency ratio method for landslide susceptibility assessment. *Landslides*, *14*(2), 727–741. https://doi.org/10.1007/s10346-016-0771-x
25. Liviona, C. D. A., Saraswati, R., Wibowo, A. (2020). The Effect of NDVI and NDBI on Land Surface Temperature in Cirebon City 2015 and 2019. *E3S Web of Conferences*, *202*. https://doi.org/10.1051/e3sconf/202020213006
26. Lu, S., Bai, X., Li, W., Wang, N. (2019). Impacts of climate change on water resources and grain production. *Technological Forecasting and Social Change*, *143*(November 2018), 76–84. https://doi.org/10.1016/j.techfore.2019.01.015
27. Mahmood, R., Pielke, R. A., Hubbard, K. G., Niyogi, D., Dirmeyer, P. A., Mcalpine, C., Carleton, A. M., Hale, R., Gameda, S., Beltrán-Przekurat, A., Baker, B., Mcnider, R., Legates, D. R., Shepherd, M., Du, J., Blanken, P. D., Frauenfeld, O. W., Nair, U. S., Fall, S. (2014). Land cover changes and their biogeophysical effects on climate. *International Journal of Climatology*, *34*(4), 929–953. https://doi.org/10.1002/joc.3736
28. Marcotullio, P. J., Keßler, C., Quintero Gonzalez, R., Schmeltz, M. (2021). Urban Growth and Heat in Tropical Climates. *Frontiers in Ecology and Evolution*, *9*(August). https://doi.org/10.3389/fevo.2021.616626
29. Marwah, S. (2014). Sumberdaya air di das Konaweha Propinsi Sulawesi Tenggara. Analysis of land use changesand water resource availability in Konaweha Watershed Southeast Sulawesi Province. *Jurnal Agroteknos*, *4*(3), 208–218.
30. McCombs, J. W., Herold, N. D., Burkhalter, S. G., Robinson, C. J. (2016). Accuracy assessment of NOAA coastal change analysis program 2006-2010 land cover and land cover change data. *Photogrammetric Engineering and Remote Sensing*, *82*(9), 711–718. https://doi.org/10.14358/PERS.82.9.711
31. Mitsuda, Y., Ito, S. (2011). A review of spatial-explicit factors determining spatial distribution of land use/land-use change. *Landscape and Ecological Engineering*, *7*(1), 117–125. https://doi.org/10.1007/s11355-010-0113-4
32. Muhammad, W., Muhammad, S., Khan, N. M., Si, C. (2020). Hydrological drought indexing approach in response to climate and anthropogenic

activities. *Theoretical and Applied Climatology*, *141*(3–4), 1401–1413. https://doi.org/10.1007/s00704-020-03227-y

33. Murthy, C. S., Laxman, B., Sesha Sai, M. V. R. (2015). Geospatial analysis of agricultural drought vulnerability using a composite index based on exposure, sensitivity and adaptive capacity. *International Journal of Disaster Risk Reduction*, *12*, 163–171. https://doi.org/10.1016/j.ijdrr.2015.01.004
34. Naghibi, S. A., Pourghasemi, H. R., Pourtaghi, Z. S., Rezaei, A. (2015). Groundwater qanat potential mapping using frequency ratio and Shannon's entropy models in the Moghan watershed, Iran. *Earth Science Informatics*, *8*(1), 171–186. https://doi.org/10.1007/s12145-014-0145-7
35. Nguyen, M. T., Nguyen, C. V., Do, H. T., Hua, H. T., Tran, T. A., Nguyen, A. D., Ala, G., Viola, F. (2021). UAV-assisted data collection in wireless sensor networks: A comprehensive survey. *Electronics 10*(21), 2603. https://doi.org/10.3390/ELECTRONICS10212603
36. Oh, H. J., Pradhan, B. (2011). Application of a neuro-fuzzy model to landslide-susceptibility mapping for shallow landslides in a tropical hilly area. *Computers and Geosciences*, *37*(9), 1264–1276. https://doi.org/10.1016/j.cageo.2010.10.012
37. Panuju, D. R., Paull, D. J., Griffin, A. L. (2020). Change detection techniques based on multispectral images for investigating land cover dynamics. *Remote Sensing*, *12*(11), 1–36. https://doi.org/10.3390/rs12111781
38. Parera, E. (2024). Province. Model perubahan penutupan lahan kelompok hutan lindung land cover change model for the Mount Sirimau protected forest group, Ambon City, *Maluku 8*(2), 137–152. https://doi.org/10.3098/jhppk.v8i2.15734
39. Pokhrel, Y., Felfelani, F., Satoh, Y., Boulange, J., Burek, P., Gädeke, A., Gerten, D., Gosling, S. N., Grillakis, M., Gudmundsson, L., Hanasaki, N., Kim, H., Koutroulis, A., Liu, J., Papadimitriou, L., Schewe, J., Müller Schmied, H., Stacke, T., Telteu, C. E., … Wada, Y. (2021). Global terrestrial water storage and drought severity under climate change. *Nature Climate Change*, *11*(3), 226–233. https://doi.org/10.1038/s41558-020-00972-w
40. Pradhan, B. (2013). A comparative study on the predictive ability of the decision tree, support vector machine and neuro-fuzzy models in landslide susceptibility mapping using GIS. *Computers and Geosciences*, *51*, 350–365. https://doi.org/10.1016/j.cageo.2012.08.023
41. Prasetyo, D. A., Suprayogi, A., Hani'ah. (2018). Analisis lokasi rawan bencana kekeringan menggunakan sistem informasi geografis di kabupaten Blora Tahun 2017. *Jurnal Geodesi Undip*, *7*(4), 314–324.
42. Putra, M. R. R., Rudiarto, I. (2018). Simulasi perubahan penggunaan lahan dengan konsep celluler automata di kota Mataram. *Jurnal Pengembangan Kota*, *6*(2), 174. https://doi.org/10.14710/jpk.6.2.174-185
43. Rahmati, O., Pourghasemi, H. R., Zeinivand, H. (2016). Flood susceptibility mapping using frequency ratio and weights-of-evidence models in the Golastan Province, Iran. *Geocarto International*, *31*(1), 42–70. https://doi.org/10.1080/10106049.2015.1041559
44. Rhee, J., Im, J., Carbone, G. J. (2010). Monitoring agricultural drought for arid and humid regions using multi-sensor remote sensing data. *Remote Sensing of Environment*, *114*(12), 2875–2887. https://doi.org/10.1016/j.rse.2010.07.005
45. Riajaya, P. D., Kadarwati, F. T., Hariyono, B., Subiyakto, Cholid, M., Research. (2024). The distribution of rainfall in areas suitable for sugarcane farming in Blitar Regency, East Java. IOP Conference Series: Earth and Environmental Science, 1377, *2nd International Conference on Food and Agricultural Sciences* 2023 12/12/2023–13/12/2023 Yogyakarta, Indonesia. https://doi.org/10.1088/1755-1315/1377/1/012012
46. Ridwan, Rasyidi, E. S., Syafri, Rahman, R., Okviyani, N., Jumadil, Ma'Rief, A. A. (2021). Assessment of the relationship between building density and urban heat island using Landsat images in Makassar City. *IOP Conference Series: Earth and Environmental Science*, *802*(1). https://doi.org/10.1088/1755-1315/802/1/012042
47. Salvacion, A. R. (2021). Mapping land limitations for agricultural land use planning using fuzzy logic approach: a case study for Marinduque Island, Philippines. *GeoJournal*, *86*(2), 915–925. https://doi.org/10.1007/s10708-019-10103-4
48. Sterling, S. M., Ducharne, A., Polcher, J. (2013). The impact of global land-cover change on the terrestrial water cycle. *Nature Climate Change*, *3*(4), 385–390. https://doi.org/10.1038/nclimate1690
49. Sujarwo, M. W., Hakim, F. L., Indarto, I. (2023). Using landsat to track land use and land cover (LULC) change from 1970 To 2020 in Mayang Watershed, East Jawa. *AIP Conference Proceedings*, *2583*(January). https://doi.org/10.1063/5.0117111
50. Sulaeman, Y., Minasny, B., McBratney, A. B., Sarwani, M., Sutandi, A. (2013). Harmonizing legacy soil data for digital soil mapping in Indonesia. *Geoderma*, *192*(1), 77–85. https://doi.org/10.1016/j.geoderma.2012.08.005
51. Supari, Muharsyah, R., Sopaheluwakan, A. (2016). Mapping drought risk in Indonesia related to El-Niño hazard. *AIP Conference Proceedings*, *1730*(May). https://doi.org/10.1063/1.4947413
52. Thamrin, P. S., Mukrimin, Suryana, S. A. (2025). Utilization of satellite imagery for drought identification and drought susceptibility maps via the

frequency ratio. *Ecological Engineering and Environmental Technology*, *26*(12), 376–392. https://doi.org/10.12912/27197050/214068

53. Triyatno, T., Rahmi, L., Anwar, S., Aulia, B., Najib, S. A. M. (2025). Projecting LULC change (2025–2039) and modeling landslide susceptibility using cellular Automata–Markov Chain (Ca–Mc) in the Kambang Watershed, West Sumatra, Indonesia. *Geographia Technica*, *21*, 19–34. https://doi.org/10.21163/gt_2026.212.01
54. Vahid, R., Aly, M. H. (2025). An Integrated CA–Markov Modeling Framework for Forecasting Land Use and Land Cover Dynamics in Arkansas, USA. *Geomatics*, *5*(4), 1–19. https://doi.org/10.3390/geomatics5040062
55. Vogt, D. J., Vogt, K. A., Gmur, S. J., Scullion, J. J., Suntana, A. S., Daryanto, S., Sigurdardóttir, R. (2016). Vulnerability of tropical forest ecosystems and forest dependent communities to droughts. *Environmental Research*, *144*, 27–38. https://doi.org/10.1016/j.envres.2015.10.022
56. Weng, Q. (2012). Remote sensing of impervious surfaces in the urban areas: Requirements, methods, and trends. *Remote Sensing of Environment*, *117*, 34–49. https://doi.org/10.1016/j.rse.2011.02.030
57. Wilhite, D. A., Sivakumar, M. V. K., Pulwarty, R. (2014). Managing drought risk in a changing climate: The role of national drought policy. *Weather and Climate Extremes*, *3*(March 2013), 4–13. https://doi.org/10.1016/j.wace.2014.01.002
58. Wu, Y., Zhang, X., Shen, L. (2011). The impact of urbanization policy on land use change: A scenario analysis. *Cities*, *28*(2), 147–159. https://doi.org/10.1016/j.cities.2010.11.002
59. Xu, L., Liu, X., Tong, D., Liu, Z., Yin, L., Zheng, W. (2022). Forecasting urban land use change based on cellular automata and the PLUS model. *Land*, *11*(5). https://doi.org/10.3390/land11050652
60. Yadav, S. K. (2023). *Land Cover Change and Its Impact on Groundwater Resources: Findings and Recommendations* (J. Tarhouni (ed.)). IntechOpen. https://doi.org/10.5772/intechopen.110311
61. Yang, F., Zhao, C., Wang, J., Liu, C., Sun, Y., Soomro, S. e. H., Hu, C. (2022). Grid-quantification study on the effect of rapid urbanization on hydrological processes. *Water Supply*, *22*(6), 5853–5872. https://doi.org/10.2166/ws.2022.202
62. Yuniasih, B., Renjani, R.A., Bintang, M. (2024). Mitigasi kekeringan di tanah pasiran perkebunan kelapa sawit dengan aplikasi Janjang Kosong Betti. *Jurnal Pengelolaan Perkebunan*, *5*(1), 7–17.
63. Zha, Y., Gao, J., Ni, S. (2003). Use of normalized difference built-up index in automatically mapping urban areas from TM imagery. *International Journal of Remote Sensing*, *24*(3), 583–594. https://doi.org/10.1080/01431160304987
64. Zhang, M., Yan, R., Gao, J., Yan, S., Yan, J. (2024). A framework for characterizing spatio-temporal variation of turbidity and drivers in the navigable and Turbid River: A case study of Xitiaoxi River. *Water (Switzerland)*, *16*(17). https://doi.org/10.3390/w16172503
65. Zhou, G., Wu, B., Li, M. (2011). Improved accuracy assessment indices for object-based high resolution remotely sensed imagery classification. *Proceedings of 2011 International Conference on Image Analysis and Signal Processing, IASP 2011*, 181–186. https://doi.org/10.1109/IASP.2011.6109025